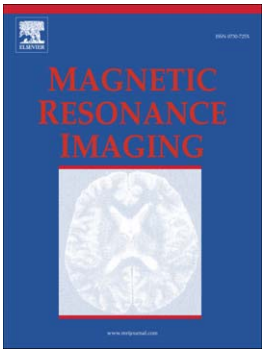

Improved l1-SPIRiT Using 3D Walsh Transform-Based Sparsity Basis

Zhen Feng, Feng Liu, Mingfeng Jiang, Stuart Crozier, He Guo, Yuxin Wang

PII: S0730-725X(14)00133-7
DOI: doi: 10.1016/j.mri.2014.04.008
Reference: MRI 8181

To appear in: *Magnetic Resonance Imaging*

Received date: 4 October 2012
Revised date: 18 March 2014
Accepted date: 12 April 2014

Please cite this article as: Feng Zhen, Liu Feng, Jiang Mingfeng, Crozier Stuart, Guo He, Wang Yuxin, Improved l1-SPIRiT Using 3D Walsh Transform-Based Sparsity Basis, *Magnetic Resonance Imaging* (2014), doi: 10.1016/j.mri.2014.04.008

Improved *l*1-SPIRiT Using 3D Walsh Transform-Based Sparsity Basis

ZHEN FENG[a], FENG LIU[b*], MINGFENG JIANG[c]

STUART CROZIER[b], HE GUO[a], YUXIN WANG[d]

[a] School of Software Technology, Dalian University of Technology, Dalian 116620, P. R. China

[b] School of Information Technology and Electrical Engineering, The University of Queensland, St Lucia, QLD 4072, Australia

[c] School of Information Science and Technology, Zhejiang Sci-Tech University, Hangzhou 310018, P. R. China

[d] School of Computer Science and Technology, Dalian University of Technology, Dalian 116624, P. R. China

Word count: 132 (Abstract) 2666 (Text)

Number of figures: 13

Number of tables: 3

Number of references: 40

Abstract

*l*1-SPIRiT is a fast magnetic resonance imaging (MRI) method which combines parallel imaging (PI) with compressed sensing (CS) by performing a joint *l*1-norm and *l*2-norm optimization procedure. The original *l*1-SPIRiT method uses two-dimensional (2D) Wavelet transform to exploit the intra-coil data redundancies and a joint sparsity model to exploit the inter-coil data redundancies. In this work, we propose to stack all the coil images into a three-dimensional (3D) matrix, and then a novel 3D Walsh transform-based sparsity basis is applied to simultaneously reduce the intra-coil and inter-coil data redundancies. Both the 2D Wavelet transform-based and the proposed 3D Walsh transform-based sparsity bases were investigated in the *l*1-SPIRiT method. The experimental results show that the proposed 3D Walsh transform-based *l*1-SPIRiT method outperformed the original *l*1-SPIRiT in terms of image quality and computational efficiency.

Keywords: MRI; Compressed Sensing; *l*1-SPIRiT; Walsh transform

1. Introduction

In conventional magnetic resonance imaging (MRI), imaging speeds are limited by the sequential acquisition of the full *k*-space data. To reduce scan duration, two different types of techniques are often used. The first one is the multiple-coil based parallel MR imaging (pMRI) schemes, which have been actively investigated over the recent years using a variety of methods [1-12]. Some of these pMRI methods require the coil sensitivities to be known explicitly, while others reconstruct images with an implicit usage of the coil sensitivity information, through an auto-calibration process. These parallel imaging techniques have been successfully implemented in routine clinical practice.

The second one is compressed sensing MR imaging (CS-MRI) [13], which exploits the sparsity of the signal in some transformation domain to reconstruct the MR images by using far fewer *k*-space data than those required for the conventional methods. Recently, a range of sparsity bases in spatial and temporal dimensions were proposed to implement the sparsifying transform, such as discrete Wavelet transform [14], discrete cosine transform [15], total variation [16], one-dimensional Fourier transform [17], KLT/PCA transform [18], singular value decomposition [19], motion estimation [20] and dictionary learning [21]. Compressed sensing (CS) method has been successfully applied in static and dynamic MRI studies.

Recently, the combination of CS and pMRI methods has been proposed for fast imaging applications. Two typical methods have been developed for the implementation of hybrid CS-pMRI. The first method performs a joint optimization procedure for the image reconstruction. For example, Sparse Sensitivity Encoding (SENSE) [22] and its equivalents [23, 24] added Wavelets and total variation as $l1$ constraints. In addition, Weller et al. [25] minimized the image sparsity term ($l1$-norm) and the data deviation ($l2$-norm) term together during GeneRalized Autocalibrating Partially Parallel Acquisitions (GRAPPA) reconstruction. This method is easy to implement, however, a major concern is the relatively poor incoherence between the sparsity basis and the encoding matrix [23]. In the second method, the CS-pMRI reconstruction was treated as a separate stage either before or after the pMRI reconstruction stage. For example, the CS-SENSE algorithm first reconstructed a set of aliased images

with a localized field-of-view for each coil by using SparseMRI [16], and then formed the final image from the aliased images using Cartesian SENSE [26]. In addition, CS-MRI reconstruction was first carried out on each coil image, then GRAPPA [27] and nonlinear GRAPPA [28] followed to reconstruct the final MR image, respectively. In [29], Auto-calibrating Reconstruction for Cartesian Sampling (ARC) parallel imaging was applied firstly, and then CS-MRI reconstruction was used independently on each coil image. These sequential methods can usually provide higher acceleration, however, noise and errors introduced in one operation can be augmented by the following procedure.

*l*1-SPIRiT [30, 31] belongs to the first set of CS-pMRI methods. In this method, as an alternative to form a large linear system, the joint optimization with multiple objective functions was proposed and the solutions were iteratively constrained to satisfy Wavelet-sparsity constraints, data fidelity and calibration consistency. This iterative projection method can largely avoid the incoherence problem between the encoding matrix and the sparsity basis.

The original *l*1-SPIRiT method enforces the sparsity penalty term in two steps. Firstly, 2D Wavelet transforms were performed on different coil images to exploit the intra-coil redundancies; secondly, a joint-sparsity model is proposed to correlate Wavelet coefficients of different coils to exploit the inter-coil redundancies. In this work, we propose to jointly exploit the intra-coil and inter-coil redundancies by stacking coil images into a 3D matrix, which facilities a 3D Walsh transform of the coil images for the follow-up CS reconstruction. As a useful signal processing way, the Walsh transform technique has been widely used in various fields. For example, the one-dimensional (1D) Walsh transform is the fundamental technique of code division multiple access (CDMA) in the wireless communication field [32]. In the CS field, the 2D Walsh transform has been used as sensing matrix in recent studies [33, 34]. In this work, the 3D Walsh transform has been developed as a novel sparsity basis for the CS-MRI application. In the rest of the paper, we first introduce the mechanism of the proposed method in terms of exploiting the intra-coil and inter-coil data redundancies, and then validate the performance of the developed sparsity basis in *l*1-SPIRiT imaging reconstruction.

2. Theory

2.1 l1-SPIRiT

The *l*1-SPIRiT method integrates CS with the auto-calibrating parallel imaging method SPIRiT to accelerate MRI signal sampling processes. To reliably reconstruct a MR image from the under-sampled k-space data collected by multiple coils, a concatenated problem is solved with a joint *l*1-Wavelet minimization, data fidelity and calibration consistency constraints:

$$minimize_m \quad Joint\, l_1(\Psi_{wavelet}(m)) \tag{1}$$

$$subject\, to \quad DFm = y \tag{2}$$

$$Gm = m \tag{3}$$

Here m refers the MR coil images to be reconstructed, y is the *k*-space data collected by multiple coils. F represents a Fourier operator for each coil image, D is a under-sampling operator for *k*-space data collection. G is the SPIRiT operator that enforces the calibration consistency. $\Psi_{wavelet}$ represents a 2D Wavelet transform operator on coil images. The 2D Wavelet transform-based joint sparsity model in Eq.(1) can be formulated as follows:

$$Joint\, l_1(w) = \sum_r \sqrt{\sum_c |w_{rc}|^2} \tag{4}$$

where $w = \Psi_{wavelet}(m)$, w_{rc} is the Wavelet coefficients, r is the coil index and c is the Wavelet coefficient index in each coil. The coefficients at the same spatial positions but from different coils are jointly penalized to protect small coefficients from being suppressed. As mentioned above, the 2D Wavelet transform $\Psi_{wavelet}$ exploits the intra-coil data redundancies and the joint-sparsity model in Eq. (4) exploits the inter-coil data redundancies.

2.2 3D Walsh transform-based sparsity basis

The 1D Walsh transform is a non-sinusoidal, orthogonal transformation technique that decomposes a signal into a set of Walsh functions [35, 36]. The Walsh functions are rectangular or square waves with values of +1 or –1. The first eight Walsh functions are defined as:

Index	Walsh function values							
0	1	1	1	1	1	1	1	1
1	1	1	1	1	-1	-1	-1	-1
2	1	1	-1	-1	-1	-1	1	1
3	1	1	-1	-1	1	1	-1	-1
4	1	-1	-1	1	1	-1	-1	1
5	1	-1	-1	1	-1	1	1	-1
6	1	-1	1	-1	-1	1	-1	1
7	1	-1	1	-1	1	-1	1	-1

For a 1D signal $f(x)$ with length I, its Walsh transform and the inverse Walsh transform are defined as:

$$w_n = \frac{1}{I}\sum_{i=0}^{I-1} f_i WAL(n,i) \tag{5}$$

$$f_i = \sum_{i=0}^{I-1} w_n WAL(n,i) \tag{6}$$

where $n = 0,1,...,I-1$ and $WAL(n,i)$ is the i-th value of the n-th Walsh function. As shown in Eq. (5), it can be seen that the Walsh coefficients are generated from the linear combination of the original signal and the predefined Walsh functions.

In our simulations, it was observed that 1D Walsh transform has effective energy concentration capabilities in the pMRI datasets. We took comparisons between the 1D Walsh transform and the two-level Daubechies Wavelet on an in vivo eight-coil brain dataset. This dataset (as shown in Figure 1) was acquire on a 1.5T GE scanner with TR = 4200 ms, TE = 85 ms, the sizes of the acquired coil images were 200 × 200 × 8 and in this work we interpolated them to 256 × 256 × 8 [12].

Figure 1

The first test was performed to compare the sparsity in the coil directions. In pMRI system, the coils are designed to maximize the difference and minimize the correlations of each coil sensitivity, therefore it becomes challenging to generate sparsity in the coil direction. In our study, as shown in Figure 1, each coil element is relatively large enough to 'see' entire field of view, although it is shaded in the far region of the image. In this case, the structural similarities between coil images still exist, and the same view has also been reported in [37] and [38]. With the existence of the inter-coil redundancies, we can then conduct sparsity transform studies. In Figure 2, the magnitudes of 64th row, 64th column pixels in multiple coil images are denoted in blue curve with squares, due to the influences of the sensitivities, the pixel magnitudes varies in the same positions of the different coil images. However, the Walsh transform (green curve with stars) can still concentrate the energies into a few large coefficients, while the Wavelet transform coefficients (red curve with circles) are on average large.

The second test was presented to compare the sparsity on one row of pixels on one coil image. In Figure 3, the blue curve with squares shows the magnitude changes of the 128th row pixels on the first coil image. The green curve with stars shows the Walsh transform coefficients and the red curve with circles shows the Wavelet transform coefficients, it can be found that the green curve decline much faster than the red curve.

Figure 2

Figure 3

For individual coil image, the 2D Walsh transform can be implemented by first performing 1D Walsh transforms on all the rows (x- direction), and second performing 1D Walsh transforms on all the columns (y- direction). Given a 2D signal $f(x,y)$ with a size of $I \times J$, the 2D Walsh transform and its inverse are formulated as:

$$w_{m,n} = \frac{1}{I \times J} \sum_{i=0}^{I-1} \left(\sum_{j=0}^{J-1} f_{i,j} WAL(n, j) \right) WAL(m, i) \tag{7}$$

$$f_{i,j} = \sum_{i=0}^{I-1} \left(\sum_{j=0}^{J-1} w_{m,n} WAL(n, j) \right) WAL(m, i) \tag{8}$$

The multiple coil images can be stacked to form a 3D matrix, then the 3D Walsh transform can be implemented by performing the sequential 1D Walsh transforms in three directions: firstly in the coil direction, secondly in the x- direction and lastly in the y- direction. In this way, given a 3D signal $f(x,y,z)$ with a size of $I \times J \times K$ the 3D Walsh transform and its inverse are formulated as:

$$w_{m,n,c} = \frac{1}{I \times J \times K} \sum_{i=0}^{I-1} (\sum_{j=0}^{J-1} (\sum_{k=0}^{K-1} f_{i,j,k} WAL(c,k)) WAL(n,j)) WAL(m,i) \quad (9)$$

$$f_{i,j,k} = \sum_{i=0}^{I-1} (\sum_{j=0}^{J-1} (\sum_{k=0}^{K-1} w_{m,n,c} WAL(c,k)) WAL(n,j)) WAL(m,i) \quad (10)$$

Figure 4 visualized the 3D Walsh coefficients slice by slice, from the top to the bottom in the coil direction. For each slice, the z-axis shows the magnitudes of the coefficients. It is observed that (a) for each slice, large coefficients concentrate on the corners; (b) the largest coefficients in each slice decrease from the top (first) slice to the bottom (eighth) slice.

Figure 4

Figure 5 compares the transform coefficients in curve views. The Wavelet coefficients, 2D Walsh coefficients and the 3D Walsh coefficients were sorted according to the magnitude and then plotted as curves. Figure 5(a) shows all the sorted transform coefficients. It is obvious that the 2D Wavelet coefficients are much larger than the 2D and 3D Walsh coefficients in the first 2×10^5 coefficients. Figure 5(b) shows the first 512 coefficients, this figure provides clear comparison between the Wavelet coefficients and Walsh coefficients. Figure 5(c) zooms in Figure (b) to compare the 2D Walsh coefficients and the 3D Walsh coefficients, it can be seen that the 3D Walsh coefficients drop faster than the 2D Walsh coefficients. Therefore, from the curve view, the 3D Walsh coefficients have the sparsest representation among the three methods, and the 2D Walsh-based representation is sparser than the Wavelet-based representation.

Figure 5

Figure 6 compares the reconstruction qualities of the first coil images using the largest 2.5×10^4, 5×10^4 and 1×10^5 coefficients. The left column shows the sparse coefficients of the 3D Walsh transform (only show the top slice, where large values concentrate), the 2D Walsh transform and the 2D Daubechies Wavelet transform on the first coil image. Figure 7 shows the corresponding error maps

in Figure 6. Serious information lost was observed in the second and third columns for the 2D Wavelet-based method, while the 2D and 3D Walsh methods can still keep most of the details. From the second column, it can also be found that image recovered from the 2D Walsh coefficients was blurrier than the image recovered from the 3D Walsh coefficients.

Figure 6

Figure 7

Suppose m is the multiple coil images, $\Psi_{walsh}(m)$ is the 3D Walsh transform which is implemented by sequential 1D Walsh transforms, the new *l*1-SPIRiT method can be formulated as:

$$minimize_m \quad l_1(\Psi_{walsh}(m)) \tag{11}$$

$$subject\,to \quad DFm = y \tag{12}$$

$$Gm = m \tag{13}$$

3. Methods and Materials

Experiments were performed on two in vivo eight-coil brain datasets and one eight-coil phantom dataset. The first brain dataset (shown in Figure 1) was acquire on a 1.5T GE scanner with TR = 4200 ms, TE = 85 ms, the sizes of the coil images were 200 × 200 × 8 and in this work we interpolated them to 256 × 256 × 8[12]. The second brain dataset (shown in Figure 8) was acquired on a 3T GE scanner (GE Healthcare, Waukesha, WI) with TR = 700 ms, TE = 11 ms, FOV = 22 × 22 cm^2, and matrix = 256 × 256 × 8 [26]. The phantom dataset was generated using the sensitivities of dataset 1 and was shown in Figure 9.

Figure 8

Figure 9

The *l*1-SPIRiT method was performed in two stages, the calibration stage and the reconstruction stage. In the calibration stage, the SPIRiT kernel size was set to be 5 × 5 and the Tykhonov regularization

parameter was set to be 0.01. In the reconstruction stage, the fast composite splitting algorithm (FCSA) method was used [39], the iteration number was set to be 50 and the weights for the sparsity regularization were optimized respectively from multiple trials.

Two sampling patterns were used (Figure 10), the Cartesian pattern that under-samples *k*-space in the phase direction only, and the radial pattern that under-samples *k*-space in both the phase and frequency directions. All the reconstructions were performed on a laptop with a 2.10 GHz Core i7 CPU, 6G memory. The reconstruction times were then recorded to measure the algorithm efficiencies. The peak signal-to-noise ratio (PSNR) was used to evaluate the image quality, which was computed as:

$$PSNR = 20\log_{10}\frac{1}{MSE}$$

Here MSE is the mean squared error between the fully-sampled dataset and the reconstructed dataset.

Figure 10

4. Results

Tables 1-3 recorded the PSNR of the reconstructed images and the runtimes in the reconstruction stages. It can be observed that the Walsh transform-based method obtained 2 to 4 dB higher PSNR than the Wavelet transform-based method, and the improvements were very robust in our various tests. In addition, the reconstruction times of the Walsh transform-based method were much shorter than the Wavelet transform-based methods. The improvements in computation efficiency benefited from the quick implementation of the 3D Walsh transform. In experiments, a typical 3D Walsh transform (including the pixel-wise multiplication with the scale maps) on a 256 × 256 × 8 matrix took only 0.26 seconds, while a batch of 2D Wavelet transforms on the same matrix took 0.98 seconds.

Figures 11-13 visualized the reconstructed images and the error maps. In most cases, the reconstructed image qualities by the Walsh transform-based method are much better than the Wavelet

transform-based method. The red arrows in the figures marked some obvious artifacts in the reconstructed images by using the 2D Wavelet transform-based method.

Table 1

Table 2

Table 3

Figure 11

Figure 12

Figure 13

5. Discussion

5.1 The utility of inter-coil similarities in CS-pMRI reconstruction

Compared with the original image, the image obtained from each coil is sensitivity weighted, that is, the coil images share same structures of the object but with varied gray scales from position to position. In the early CS-pMRI works, this image similarity was not effectively exploited. The sequential methods [27,28,29] first reconstructed each coil image in the CS stage; then the joint optimization methods was proposed to construct the whole image, but each coil image was still sparsified by 2D sparsity bases. In this work, we stacked coil images as a 3D matrix and then a 3D Walsh transform was applied to explore the data similarity between the coil images. As a new sparsity basis, the 3D Walsh transform makes use of both the intra-coil and inter-coil redundancies information, facilitating the CS reconstruction of array coil based imaging.

5.2 The 3D Walsh transform-based sparsity basis: a time-efficient way for reconstruction

As shown in Tables 1, 2 and 3, the proposed Walsh transform-based method is capable of achieving equivalent or superior reconstruction qualities to the original Wavelet transform-based method. The proposed method is quite robust in terms of reconstructed image qualities under various experimental

settings. Another obvious advantage of the proposed method is its computational efficiency. The experiments have shown that for a reconstruction of the same size, the proposed method is around 4 times faster than the original method. It has been well acknowledged that the CS-MRI reconstruction is quite time-consuming, while the proposed method can save a great deal of time without sacrificing reconstructed image qualities. This computational efficiency is important for the practical application of CS-MRI in clinical settings.

5.3. Extensions of the 3D Walsh transform-based sparsity basis to other CS-MRI methods

Although here we only tested the 3D Walsh transform-based sparsity basis on *l*1-SPIRiT, it is quite straightforward to apply the proposed sparsity basis to other CS-MRI applications, such as the joint method Sparse SENSE [22] and the sequential method CS-SENSE [23]. In the future, the 3D Walsh transform scheme can also be investigated in the dynamic imaging method to generate inter-frame sparse representations [40].

6. Conclusion

In the CS-pMRI scheme, the sparsity of the MR coil images play an important role in image reconstruction. Conventional 2D Wavelet transforms are limited in sparsifying individual coil images, without making use of the correlations between coil images. In this work, the 3D Walsh transform-based sparsity was proposed to implement CS-pMRI reconstruction. The experimental results showed that the proposed method was capable of reconstructing the MR image with better quality and less reconstruction time than the original method. In the future work, we will extend the Walsh transform-based method for other CS-MRI applications.

References

[1] Sodickson DK, Manning WJ. Simultaneous acquisition of spatial harmonics (smash): fast imaging with radiofrequency coil arrays. Magn Reson Med 1997; 38 (4): 591–603.

[2] Pruessmann KP, Weiger M, Scheidegger MB, Boesiger P. SENSE: sensitivity encoding for fast MRI. Magn Reson Med 1999; 42: 952–962.

[3] Kyriakos W, Panych L, Kacher D, Westin C, Bao S, Mulkern R, Jolesz F. Sensitivity profiles from an array of coils for encoding and reconstruction in parallel (SPACE RIP). Magn Reson Med 2000; 44: 301–308.

[4] Yeh E, McKenzie C, Ohliger M, Sodickson D. Parallel magnetic resonance imaging with adaptive radius in k-space (PARS): constrained image reconstruction using k-space locality in radiofrequency coil encoded data. Magn Reson Med 2005; 53:1383–1392.

[5] Liu C, Bammer R, Moseley M. Parallel imaging reconstruction for arbitrary trajectories using k-space sparse matrices (kSPA). Magn Reson Med 2007; 58:1171–1181.

[6] Jakob PM, Griswold MA, Edelman RR, Sodickson DK. AUTO-SMASH, a self-calibrating technique for SMASH imaging. Proc ISMRM Sydney 1998; 1975.

[7] Griswold MA, Jakob P, Nittka M, Goldfarb J, Haase A. Partially parallel imaging with localized sensitivities (PILS). Magn Reson Med 2000; 44:602–609.

[8] Griswold MA, Jakob PM, Heidemann RM, Nittka M, Jellus V, Wang J, Kiefer B, Haase A. Generalized autocalibrating partially parallel acquisitions (GRAPPA). Magn Reson Med 2002; 47:1202–1210.

[9] Beatty PJ. Reconstruction methods for fast magnetic resonance imaging. PhD thesis, Stanford University. 2006.

[10] Ying L, Sheng J. Joint image reconstruction and sensitivity estimation in SENSE (JSENSE). Magn Reson Med 2007; 57:1196–1202.

[11] Beatty PJ, Brau AC, Chang S, Joshi SM, Michelich CR, Bayram E, Nelson TE, Herfkens RJ, Brittain JH. A Method for autocalibrating 2-d accelerated volumetric parallel imaging with clinically practical reconstruction times. Proc ISMRM Berlin 2007; 1749.

[12] Lustig M, Pauly JM. SPIRiT: Iterative self-consistent parallel imaging reconstruction from arbitrary –space. Magn Reson Med 2010; 64 (2): 457–471.

[13] Donoho DL. Compressed sensing. IEEE Trans Inf Theory 2006; 52 (4): 1289–1306.

[14] Mallat S G. A Wavelet Tour of Signal Processing 2nd edn. New York: Academic Press, 1999.

[15] Ahmed N, Natarajan T, Rao KR. Discrete cosine transfom. IEEE Trans Comput 1974; 23: 90–93.

[16] Lustig M, Donoho DL, Pauly JM. Sparse MRI: The application of compressed sensing for rapid MR imaging. Magn Reson Med 2007; 58 (6): 1182–1195.

[17] Lustig M, Santos JM, Donoho DL, Pauly JM. k-t SPARSE: High frame rate dynamic MRI exploiting spatio-temporal sparsity. Proc ISMRM Seattle WA 2006.

[18] Jung H, Ye JC, Kim EY. Improved k-t BLAST and k-t SENSE using FOCUSS. Phys Med Biol 2007; 52: 3201–3226.

[19] Hong M, Yu Y, Wang H, Liu F, Crozier S. Compressed sensing MRI with singular value decomposition-based sparsity basis. Phys Med Biol 2011; 56: 6311-6325.

[20] Jung H, Sung K, Nayak KS, Kim EY, Ye JC. k-t FOCUSS: A general compressed sensing framework for high resolution dynamic MRI. Magn Reson Med 2009; 61 (1): 103–116.

[21] Chen XYY, Huang F. A novel method and fast algorithm for MR image reconstruction with significantly under-sampled data. Inverse Probl Imag 2010; 4(2): 223–240.

[22] Liu B, Sebert FM, Zou Y, Ying L. Sparse SENSE: randomly-sampled parallel imaging using compressed sensing. Proc ISMRM Toronto, Ontario, Canada 2008; 3154.

[23] Liang D, Liu B, Ying L. Accelerating sensitivity encoding using compressed sensing. Proc IEEE Eng Med Biol Soc, Vancouver 2008; 1667–1670.

[24] Block KT, Uecker M, Frahm J. Undersampled radial MRI with multiple coils. Iterative image reconstruction using a total variation constraint. Magne Reson Med 2007; 57 (6): 1086–1098.

[25] Weller DS, Polimeni JR, Grady LJ, Wald LL, Adalsteinsson E, Goyal VK. Combining nonconvex compressed sensing and GRAPPA using the nullspace method. Proc ISMRM Stockholm Sweden 2010; 4880.

[26] Liang D, Liu B, Wang J, Ying L. Accelerating SENSE using compressed sensing. Magn Reson Med 2009; 62: 1574–1584.

[27] Fischer A, Seiberlich N, Blaimer M, Jakob PM, Breuer FA, Griswold MA. A Combination of Nonconvex Compressed Sensing and GRAPPA (CS-GRAPPA). Proc ISMRM Honolulu Hawai'i USA 2009; 2813.

[28] Chang YC, King KF, Liang D, Ying L. Combining Compressed Sensing And Nonlinear Grappa For Highly Accelerated Parallel MRI. Proc ISMRM Melbourne Victoria Australia 2012; 2219.

[29] Beatty PJ, King KF, Marinelli L, Hardy CJ, Lustig M. Sequential Application of Parallel Imaging and Compressed Sensing. Proc ISMRM Honolulu Hawai'i USA 2009; 2824.

[30] Lustig M, Alley M, Vasanawala S, Donoho DL, Pauly JM. *l*1-SPIRiT: Autocalibrating parallel imaging compressed sensing. Proc ISMRM Honolulu Hawai'i USA 2009; 379.

[31] Murphy M, Alley M, Demmel J, Keutzer K, Vasanawala S, Lustig M. Fast *l*1-SPIRiT compressed sensing parallel imaging MRI: scalable parallel implementation and clinically feasible runtime. IEEE Trans Med Imag 2012; 31(6): 1250-1262.

[32] Swales SC, Busby T, Purle DJ, Beach MA, McGeehan JP. Comparison of CDMA techniques for third generation mobile radio systems. IEEE Veh Technol Conf Secaucus NJ USA 1993; 424-427.

[33] Li C, Sun T, Kelly K, Zhang Y. A compressive sensing and unmixing scheme for hyperspectral data processing. IEEE Trans Image Process 2012; 21(3):1200-1210.

[34] Jiang H, Deng W, Shen Z. Surveillance Video Processing Using Compressive Sensing. Inverse Probl Imaging 2012; 6(2): 201-214.

[35] Geadah YA. Natural, Dyadic, and Sequency Order Algorithms and Processors for the Walsh-Hadamard Transform. IEEE Trans Comput 1977; 26(5): 435-442.

[36] Pearl J. Time, Frequency, Sequency, and their Uncertainty Relations. IEEE Trans Inf Theory 1973; 19(2): 225-229.

[37] Majumdar A, Chaudhury KN, Ward R. Calibrationless Parallel Magnetic Resonance Imaging: A Joint Sparsity Model. Sensors 2013; 13: 16714-16735. doi:10.3390/s131216714

[38] Cesar FC and Andrzej C. Multidimensional compressed sensing and their applications. WIREs Data Mining Knowl Discov2013. doi: 10.1002/widm.1108

[39] Huang J, Zhang S, Metaxas D. Efficient MR image reconstruction for compressed MR imaging. Med. Image Anal. 2011; 15(5): 670-679.

[40] Majumdar A .Motion predicted online dynamic MRI reconstruction from partially sampled k-space data. Magn Reson Imaging 2013; http://dx.doi.org/10.1016/j.mri.2013.06.003

Figure 1. The fully-sampled combined image and eight coil images (dataset 1).

Figure. 2 Energy concentration capability comparisons between the Walsh transform and the Wavelet transform in the coil direction.

Figure. 3 Energy concentration capability comparisons between the Walsh transform and the Wavelet transform on one row of individual coil image.

Figure 4. 3D Walsh coefficients for eight coil images. The logarithmic computation log(1+double(w)) was used to stretch the magnitudes of Walsh coefficients for better visualization.

Figure 5. The sorted coefficients for 2D Wavelet, 2D Walsh and 3D Walsh transform. (a) All the sorted transform coefficients. The coefficients amount to $256\times256\times8=524288$ for the eight-coil dataset 1. (b) The first 512 large sorted transform coefficients. (c) The zoomed-in comparison between the 2D and 3D Walsh coefficients.

Figure 6 The reconstructed images from subset of the largest 2.5×10^4, 5×10^4 and 1×10^5 transform coefficients using the 3D Walsh transform, the 2D Walsh transform and the 2D Wavelet transform.

Figure 7 The error maps between the fully-sampled image and the reconstructed images from subset of the largest 2.5×10^4, 5×10^4 and 1×10^5 transform coefficients using the 3D Walsh transform, the 2D Walsh transform and the 2D Wavelet transform. For the fourth column, the error maps were magnified 10 times for clear visualization.

Figure 8. The fully-sampled combined image and eight coil images (dataset 2).

Figure 9. The fully-sampled combined image and eight coil images (phantom).

Figure 10 Sampling patterns. Left column: Cartesian sampling pattern. Right column: radial sampling pattern.

Figure 11 Reconstructed images and error maps for dataset 1 with reduction 4. First column: 2D Wavelet transform-based method using Cartesian trajectories. Second column: 3D Walsh transform-based method using Cartesian trajectories. Third column: 2D Wavelet transform-based method using radial trajectories. Fourth column: 3D Walsh transform-based method using radial trajectories.

Figure 12 Reconstructed images and error maps for dataset 2 with reduction 4. First column: 2D Wavelet transform-based method using Cartesian trajectories. Second column: 3D Walsh transform-based method using Cartesian trajectories. Third column: 2D Wavelet transform-based method using radial trajectories. Fourth column: 3D Walsh transform-based method using radial trajectories.

Figure 13 Reconstructed images and error maps for phantom with reduction 4. First column: 2D Wavelet transform-based method using Cartesian trajectories. Second column: 3D Walsh transform-based method using Cartesian trajectories. Third column: 2D Wavelet transform-based method using radial trajectories. Fourth column: 3D Walsh transform-based method using radial trajectories.

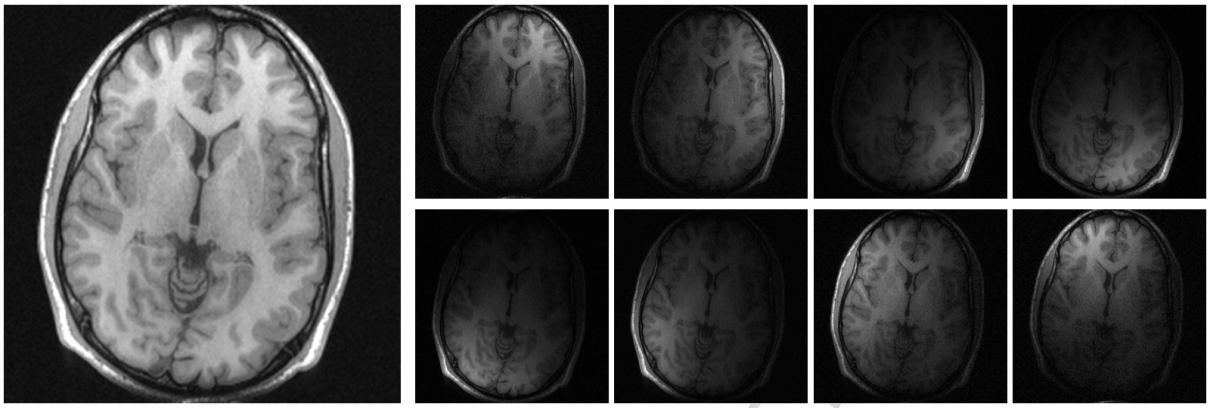

Figure 1

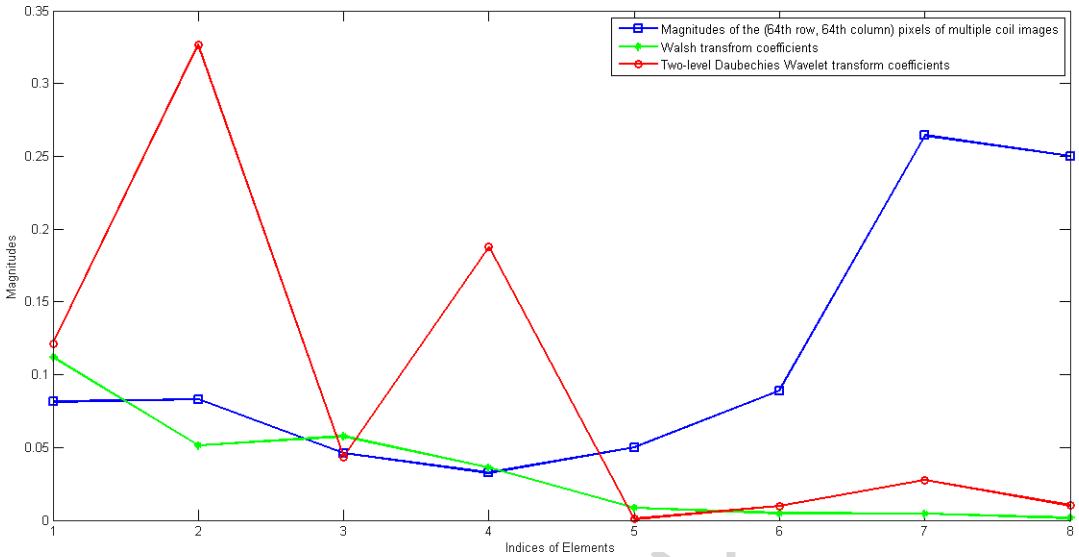

Figure 2

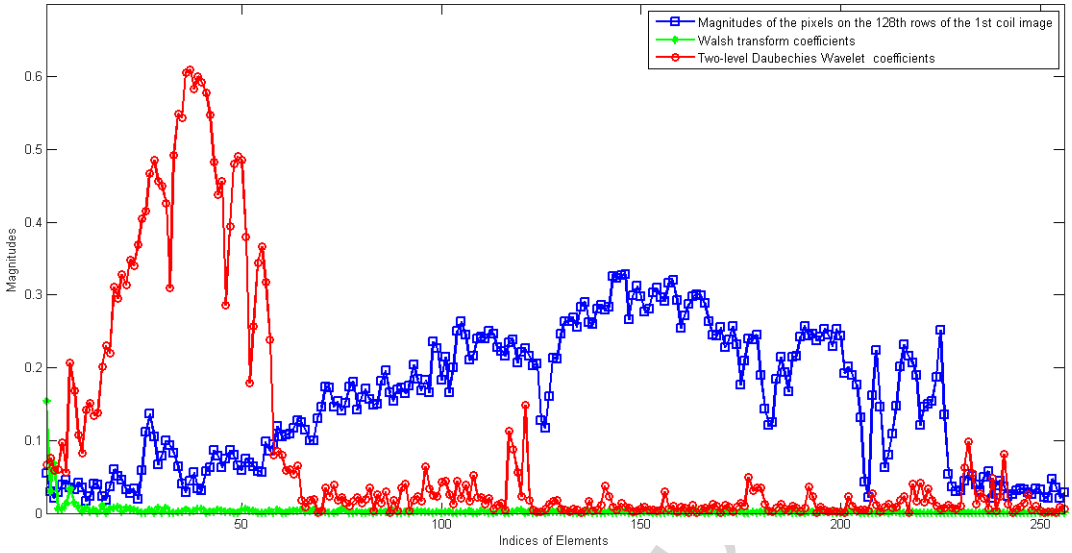

Figure 3

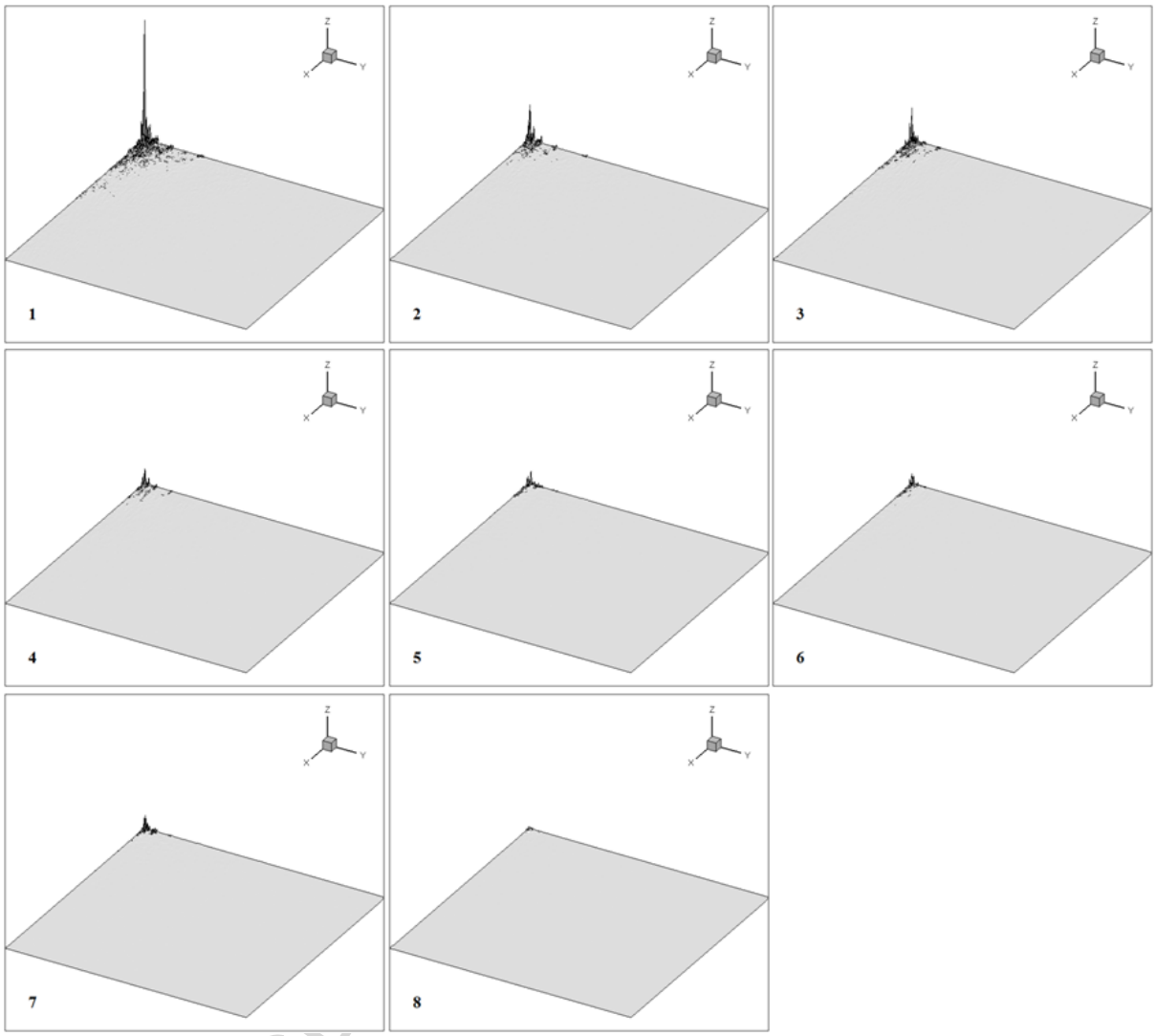

Figure 4

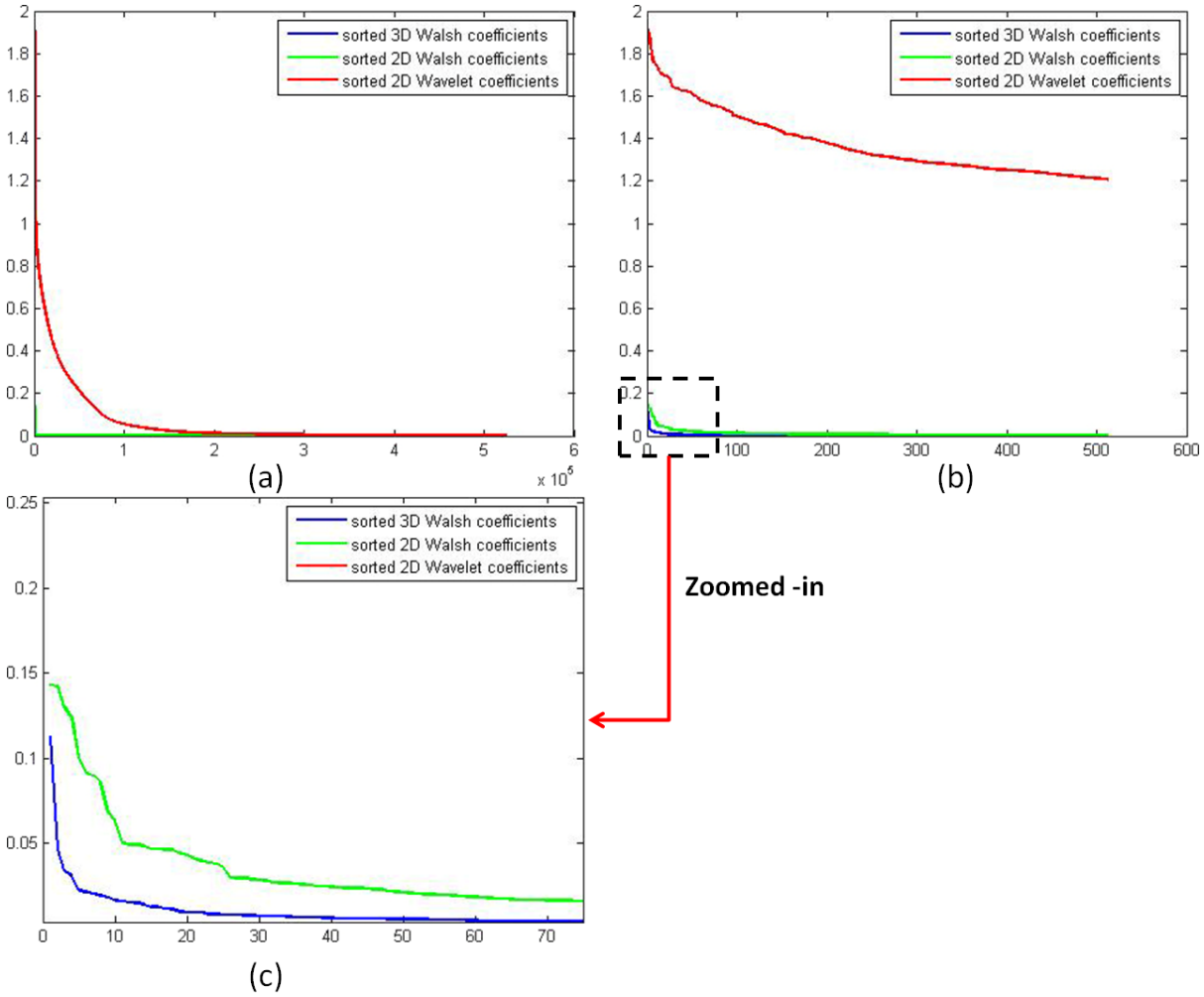

Figure 5

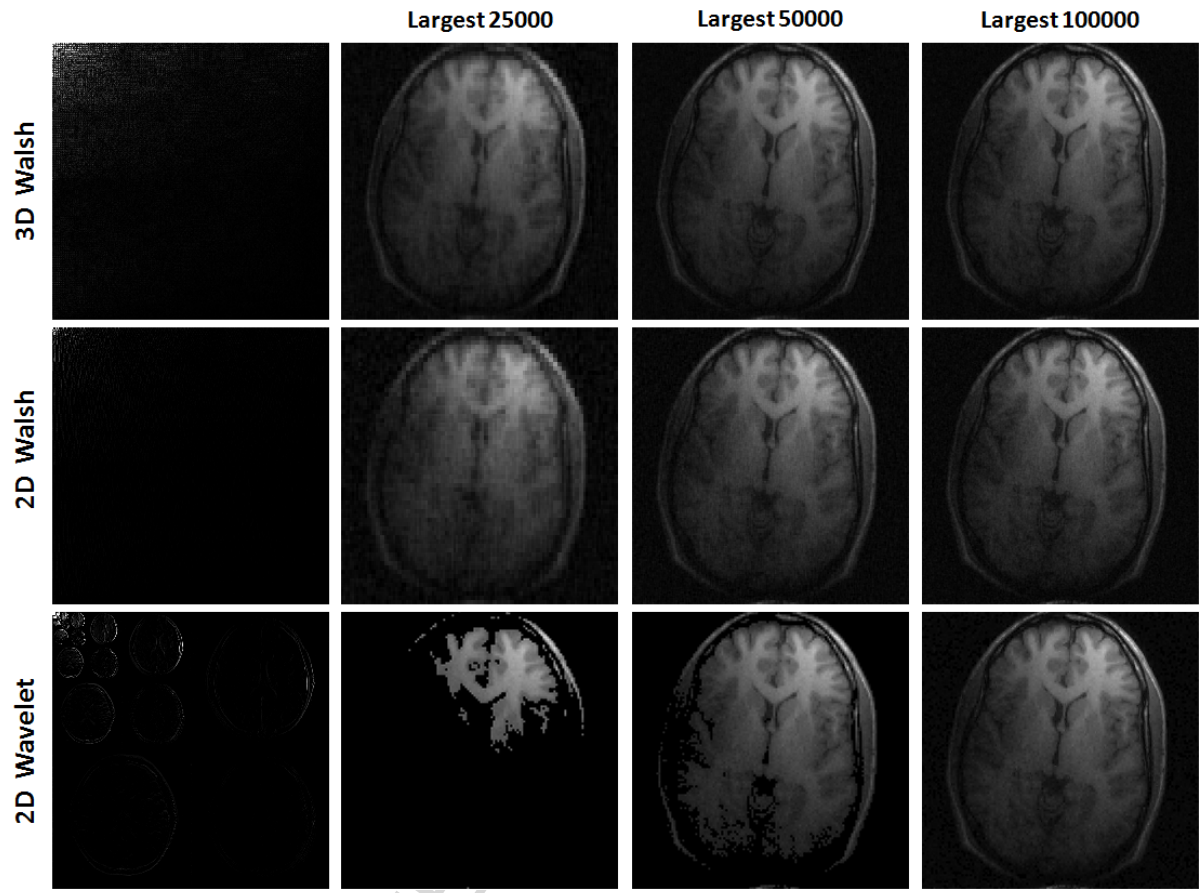

Figure 6

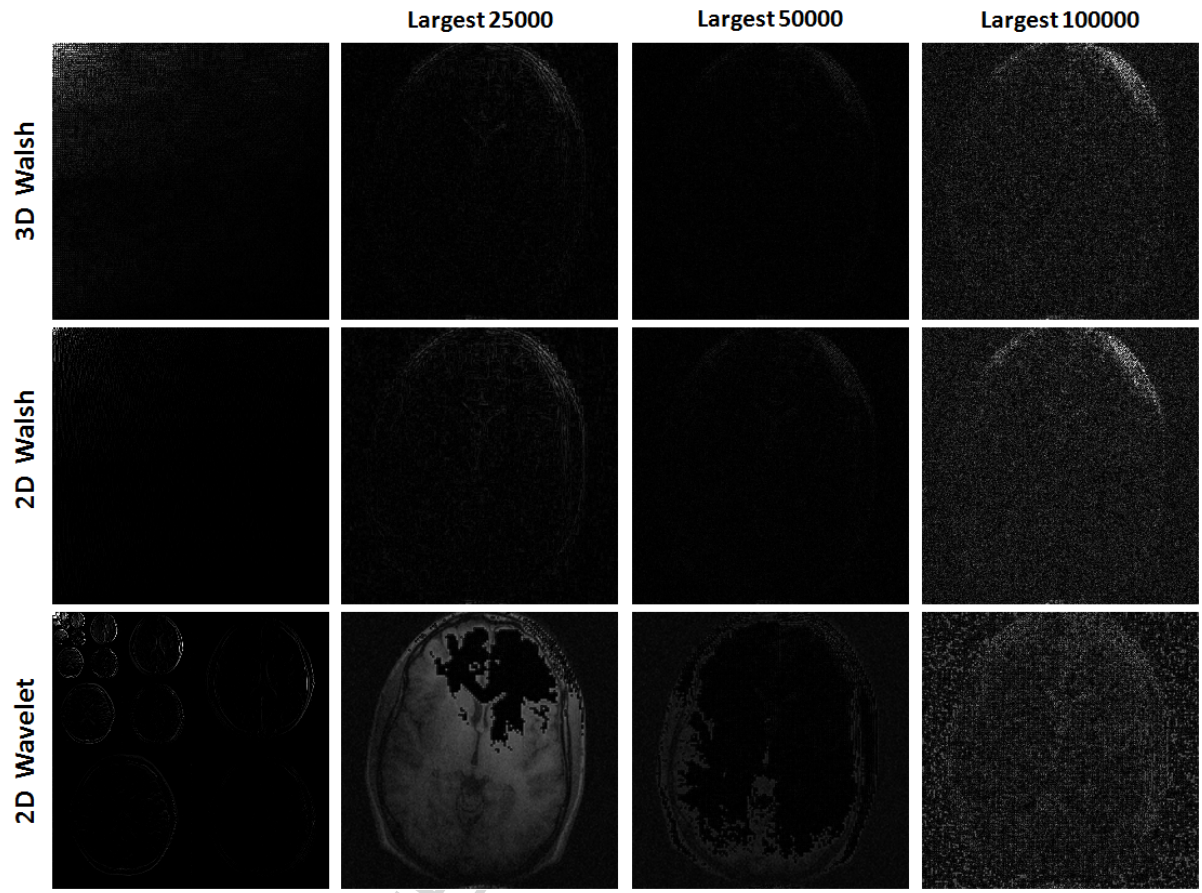

Figure 7

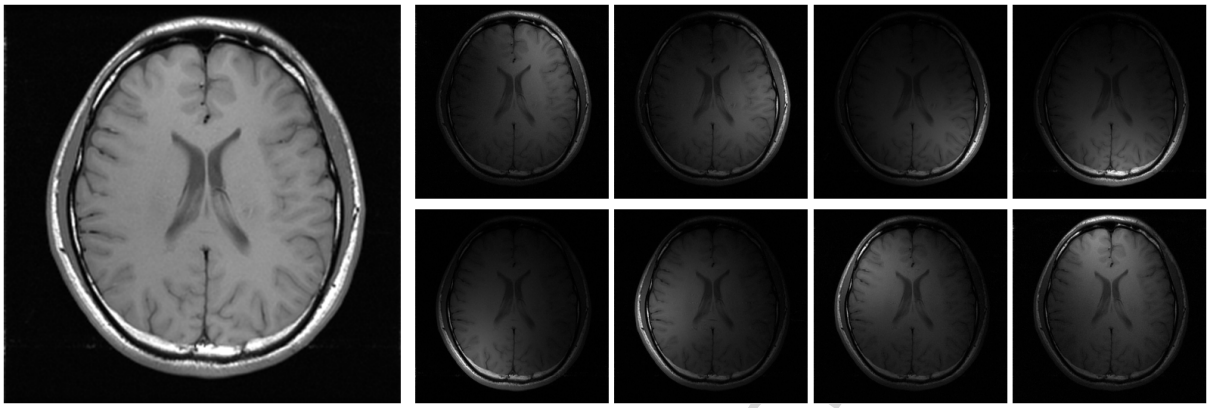

Figure 8

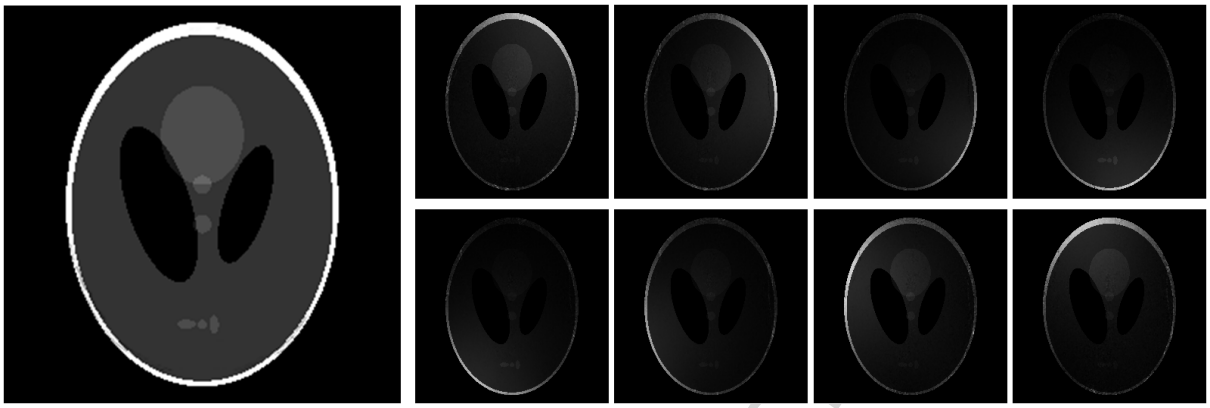

Figure 9

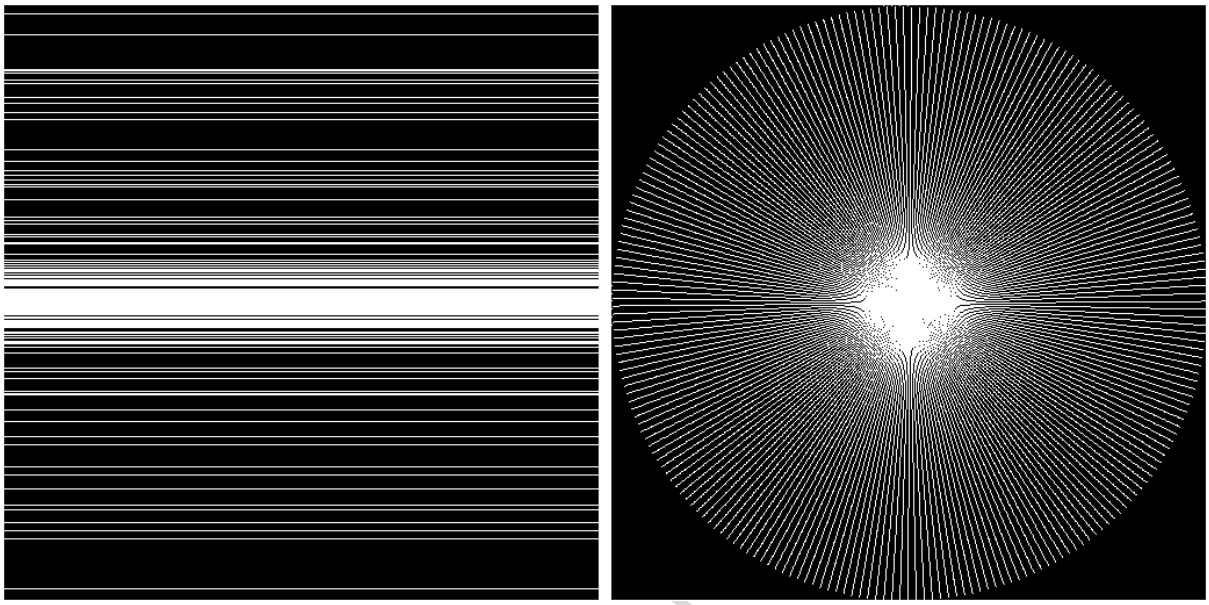

Figure 10

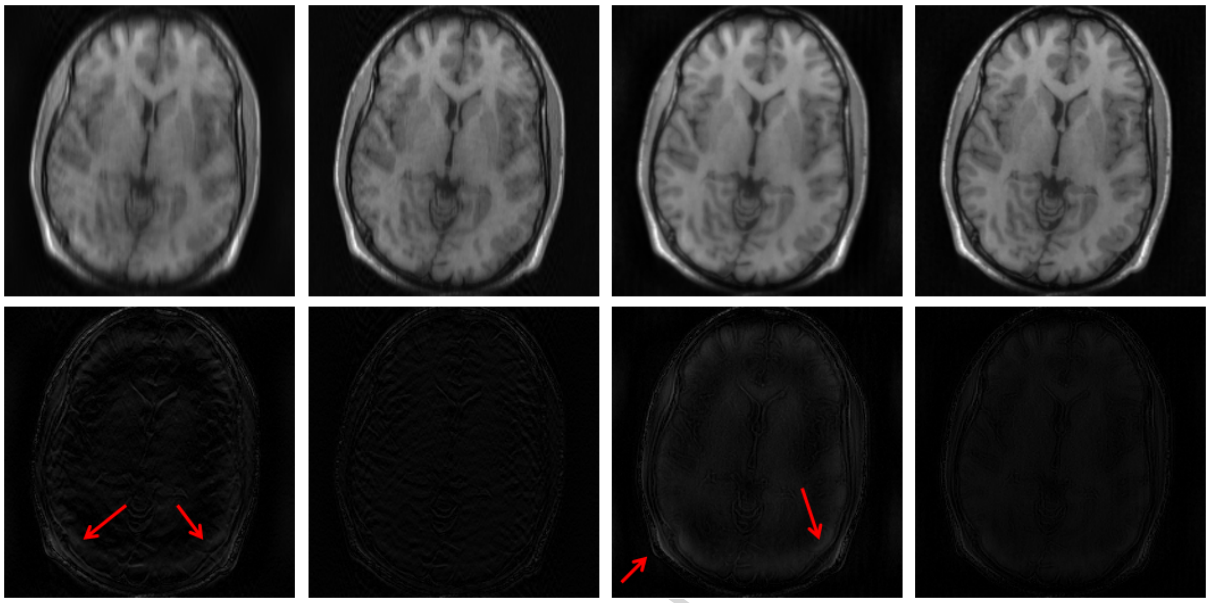

Figure 11

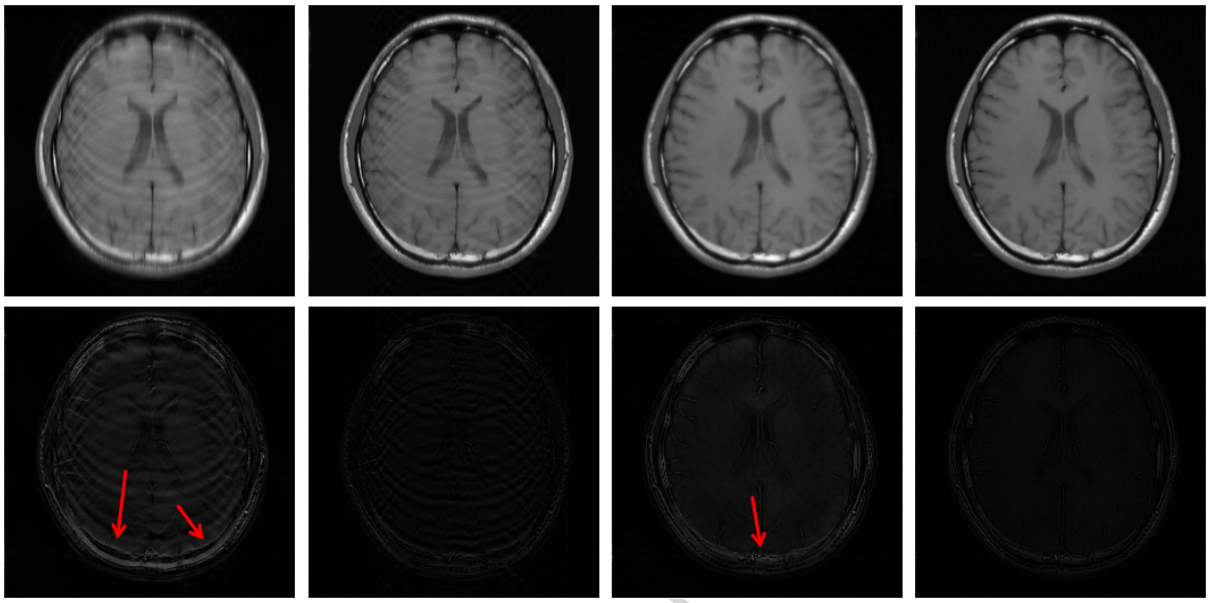

Figure 12

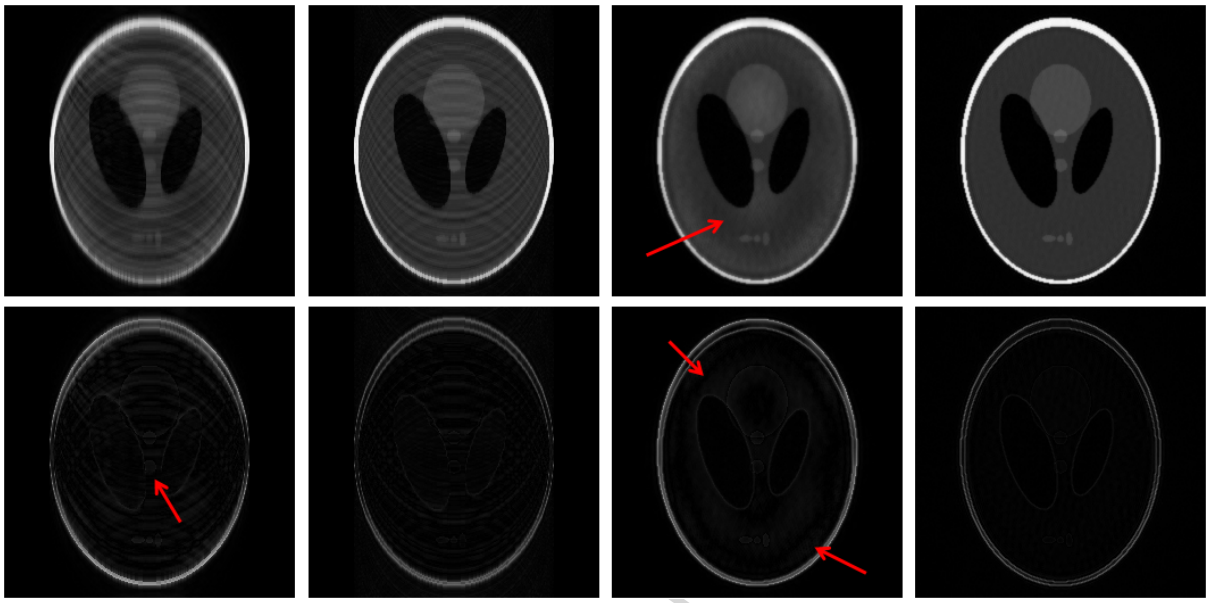

Figure 13

Table 1. Reconstruction performance for dataset 1.

Sampling Patterns	Reduction Factor	Methods	PSNR (dB)	Runtime (s)
Cartesian	3	Walsh	30.23	62.98
		Wavelet	28.08	193.49
	4	Walsh	27.26	65.77
		Wavelet	26.49	196.19
Radial	3	Walsh	28.84	63.87
		Wavelet	26.96	221.19
	4	Walsh	28.71	60.08
		Wavelet	24.85	217.99

Table 2. Reconstruction performance for dataset 2.

Sampling Patterns	Reduction Factor	Methods	PSNR (dB)	Runtime (s)
Cartesian	3	Walsh	30.82	65.23
		Wavelet	26.27	188.21
	4	Walsh	25.48	66.34
		Wavelet	23.25	187.58
Radial	3	Walsh	32.40	65.01
		Wavelet	29.22	197.61
	4	Walsh	28.71	65.88
		Wavelet	26.01	196.86

Table 3. Reconstruction performance for the phantom dataset.

Sampling Patterns	Reduction Factor	Methods	PSNR (dB)	Runtime (s)
Cartesian	4	Walsh	24.74	66.59
		Wavelet	23.44	196.98
	5	Walsh	22.66	67.89
		Wavelet	20.94	198.67
Radial	4	Walsh	27.06	68.83
		Wavelet	23.49	196.36
	5	Walsh	25.70	68.79
		Wavelet	22.69	197.86